Task-Relevant Haptic Feedback Enhances de novo Acquisition of Novel Arm Control

Abbreviated title: Haptic Feedback Enhances de novo Control

Ian S. Howard[1*] and Laura Alvarez-Hidalgo[2]

[1]School of Engineering, Computing and Mathematics, University of Plymouth, Plymouth, United Kingdom.
ORCID ID: 0000-0002-6041-9669

[2]School of Engineering, Computing and Mathematics, University of Plymouth, Plymouth, United Kingdom.
ORCID ID: 0009-0002-2068-3390

*Correspondence should be sent to:
Ian S. Howard,
School of Engineering, Computing and Mathematics, University of Plymouth, Plymouth, United Kingdom.
ORCID ID: 0000-0002-6041-9669
Email: ian.howard@plymouth.ac.uk
Telephone: +44 1752 586324

Keywords: de novo, motor learning, bimanual, novel kinematics, 2D planar arm, dynamic learning.

Number of figures: 6
Number of tables: 0
Number of words for Abstract: 200
Number of words for Introduction: 693
Number of words for Discussion: 1258

AI use statement

The authors used ChatGPT solely as a general research aid for language editing and for identifying potentially relevant literature. All scientific content, interpretations, and references were selected, verified, and entered by the authors.

Conflict of Interest

The authors declare that they have no financial, personal, or professional interests that could be construed to have influenced the paper.

Abstract (200)

The human motor system can learn to control novel effectors, but the contribution of task-relevant haptic dynamics to de novo learning remains unclear. Using a bimanual robotic interface, participants learned over two days to control the shoulder and elbow angles of a virtual arm in order to achieve accurate endpoint movements via constrained handle motions. On Day 1, one group practiced a purely kinematic mapping, whereas another group received continuous haptic feedback generated by an endpoint mass. With practice, movements shifted from sequential to more coordinated control and trajectories became straighter, with reduced directional deviation during target-directed endpoint movements, particularly in the haptic-feedback group. On Day 2, both groups learned to compensate for a velocity-dependent force field: trajectories were initially curved but straightened with practice, and washout produced after-effects. Prior haptic training led to more complete error reduction while maintaining robust after-effects. These benefits reflected a higher asymptotic level of predictive compensation in the haptic feedback condition, rather than an increased learning rate. Together, these results indicate that learning with task-relevant haptic dynamics shapes control policies for novel kinematic and dynamic relationships, enhancing subsequent sensorimotor adaptation by improving the quality and completeness of predictive control rather than simply accelerating learning.

Introduction (693)

Humans can master intricate motor skills, from rudimentary tool use to the operation of complex machinery [1–4]. Nevertheless, many motor control studies have examined relatively simple adaptations to altered task dynamics or visual feedback, often interpreted as recalibrations of existing sensorimotor mappings rather than the acquisition of fundamentally new control policies. In particular, numerous motor learning studies use veridical feedback from point-to-point movement tasks, often without kinematic transformations, and focus primarily on steady-state performance. As a result, comparatively less is known about how entirely novel movement–outcome mappings are acquired de novo, particularly when both kinematic and dynamic relationships are altered simultaneously. For example, numerous studies have investigated visuomotor adaptation [5–8], whereas dynamic learning tasks have been examined either directly [9–12] or across different unimanual contexts [13–15] and bimanual contexts [16–20].

Simultaneous visuomotor and dynamic adaptations have been investigated. For instance, participants can learn visuomotor rotations, viscous curl-fields, or their combination within the same session [21], and evidence suggests that separate yet coexisting kinematic and dynamic internal models can be formed [22]. However, such studies typically involve perturbations applied to otherwise well-learned motor tasks,

rather than the acquisition of a fundamentally novel mapping from motor commands to task-relevant states.

There has also been compelling research into more complex adaptations, such as nonlinear visuomotor transformations involving movement in altered visual space [23], mirror reversal compensations [24], rotational adaptations [25], and sensorimotor transformations [26,27]. These paradigms increasingly blur the distinction between adaptation and de novo learning, yet often remain dominated by changes in visual feedback.

More complex remapping has been investigated using finger motions to control the joint angles of a simulated planar two-link arm, demonstrating relevance for prosthetic control [28,29]. These studies have highlighted the pivotal role of visual feedback [29] in learning to control virtual objects via finger movements [30].

What remains unknown is how such remapping proceeds when visual feedback is insufficient and task-relevant dynamics must be learned. Skill acquisition that requires entirely new mappings, rather than incrementally adjusting existing ones, is often referred to as de novo learning [31–33]. Such paradigms shift the focus to the acquisition of novel movement–outcome mappings that cannot be expressed as simple parametric recalibrations of previously learned control policies. Accordingly, whereas adaptation tasks may primarily involve updating parameters within an existing internal model, de novo learning requires the construction of qualitatively new sensorimotor mappings that go beyond prior control structures. Empirical evidence suggests that early phases of de novo learning are characterized by increased motor variability, reflecting exploratory behavior and uncertainty about the appropriate control policy. There is also an initial reliance on cognitive strategies, followed by the gradual emergence of more stable and automatic control policies through trial-and-error learning over practice [32,33].

Here, we investigate de novo learning of kinematic and dynamic relationships using a virtual two-dimensional planar arm learned either with or without task-relevant haptic feedback. The arm was implemented using a bimanual robotic manipulandum. Participants controlled the simulated arm by moving two robotic handles backward and forward through two distinct one-dimensional channels. These hand movements directly controlled the angles of the shoulder and elbow joints, thereby determining the position of the end-effector. Participants were tasked with performing center-out and out-back movements, which provided a well-structured framework to quantify changes in performance and control strategies with practice.

We examined two conditions: training either with or without an endpoint mass attached to the virtual arm's end-effector, allowing us to assess how exposure to different dynamic environments and the resulting haptic feedback shape the acquisition of novel kinematic and dynamic mappings. The endpoint-mass manipulation was not

intended to replicate the velocity-dependent forces encountered in the curl-field phase. Instead, it provided structured, task-relevant dynamic feedback during the acquisition of the novel movement-outcome mapping. This allowed us to ask whether learning a new control policy in the presence of physically meaningful dynamics influences how subsequently encountered, unpredictable dynamics are handled.

In both scenarios, after participants became proficient at controlling the two-dimensional arm, we evaluated their adaptation to the introduction of additional novel task dynamics, specifically a velocity-dependent curl-field, thereby enabling us to probe how prior learning history influences subsequent sensorimotor adaptation.

Materials and Methods

Participants

We recruited 16 healthy, right-handed human participants from a similar age range and educational background and randomly allocated each participant to one of two experiments. All participants provided written informed consent, and the protocol was approved by the University of Plymouth's local ethics committee; all procedures were conducted in accordance with relevant guidelines and regulations. All participants completed the Edinburgh Handedness Inventory [34] and the Quick Physical Activity Rating (QPAR) assessment [35].

Experiment 1 (Kinematic Arm Task) comprised eight participants (4 female, 4 male; mean ± SD age 20.8 ± 1.4 years; QPAR 40.9 ± 19.4).

Experiment 2 (Endpoint Mass Task) included eight participants (3 female, 5 male; mean ± SD age 21.9 ± 3.2 years; QPAR 46.3 ± 16.3).

To avoid experimental bias, participants were kept naïve to the hypotheses of the study.

Experimental Setup

All experiments were conducted using two identical custom-built, back-drivable vBOT planar robotic manipulanda (Fig. 1A, B), which exhibit low mass at their handles [36]. Handle position was sampled with optical encoders at 1 kHz, and planar forces were updated by torque motors at the same rate. A planar virtual reality projection system was used to overlay images of targets, the end-effector cursor, and the 2D arm configuration in the plane of the vBOTs' movements. Participants were prevented from viewing their arms directly and were seated in front of the apparatus, holding one robot handle in each hand.

Two-joint Revolute Arm Simulation

We modeled a planar, two-joint (shoulder – elbow) revolute arm (Fig. 1C) with a workspace origin at point (0, 0). The shoulder joint was located at coordinates (−12, −2) cm, while both arm links were 12 cm in length and depicted as yellow lines with a width of 2 mm. The shoulder and elbow joints were drawn as yellow circles with a radius of 0.5 cm. The end-effector position, located at the endpoint of the second arm segment, was drawn as a red circle with a radius of 0.5 cm. The default arm configuration was purely kinematic, exhibiting no intrinsic dynamics; task-specific dynamics were introduced as required by the experimental conditions.

Participants controlled the arm by moving the left and right handles on the vBOT manipulandum, causing the simulated arm to rotate about its shoulder and elbow joints and thereby determining the location of the end–effector. To accentuate the novelty of the mapping, handle positions and joint angles were deliberately decoupled from intuitive endpoint motion. Consequently, the arm movement directional mapping, represented by the parameter dir_{slider}, was set to -1, such that outward movements of the handles tended to generate inward movement of the cursor.

Mechanical Channels

The movement of the two vBOT handles was restricted to linear channels aligned with the y-axis, with a length (*chanLen*) of 30 cm. To spatially separate the hands, the left and right channels were offset laterally by ±10 cm, yielding central handle positions at (-10, 0) cm and (+10, 0) cm, respectively.

Simulated mechanical channels constrained hand motion to a single degree of freedom along the y-axis [37], with a wall stiffness of k_{chan} = 4,000 N.m^{-1} and a damping coefficient b_{chan} = 30 N.s.m^{-1}. Forces experienced by each hand within the channels were determined by the following expression:

$$\begin{bmatrix} F_{xh} \\ F_{yh} \end{bmatrix} = k_{chan} \begin{bmatrix} -1 & 0 \\ 0 & 0 \end{bmatrix} \begin{bmatrix} x_h - x_o \\ y_h \end{bmatrix} + b_{chan} \begin{bmatrix} -1 & 0 \\ 0 & 0 \end{bmatrix} \begin{bmatrix} \dot{x}_h \\ \dot{y}_h \end{bmatrix} \quad (1)$$

which relates the forces experienced at a given handle, $[F_{xh} \quad F_{yh}]^T$, to its position relative to the channel, $[x_h - x_o \quad y_h]^T$, where [x_h , y_h] denotes the handle position, x_0 is the x-location of the channel, and the corresponding handle velocity is $[\dot{x}_h \quad \dot{y}_h]^T$.

Control of the Simulated Arm

The y-position (y) of each handle was linearly mapped to the corresponding joint angle (θ):

$$\theta = \theta_{min} + (\theta_{max} - \theta_{min}) \frac{\left(dir_{slider} \cdot y + \frac{\text{chanLen}}{2}\right)}{\text{chanLen}} \tag{2}$$

where chanLen is the length of the channel, and dir_{slider} sets the direction in which the slider acts (taking a value of 1 or -1). The y-location of the left handle, y_{h1}, was mapped to the shoulder joint angle, θ_1, over the range of $\theta_{min} = 0$ radians and $\theta_{max} = \pi$ radians:

$$\theta_1 = \frac{(15 - y_{h1})}{30}\pi \tag{3}$$

The y-location of the right handle y_{h2} was mapped to a joint angle θ_2, between the range of $\theta_{min} = -\pi$ radians and $\theta_{max} = 0$ radians:

$$\theta_2 = \frac{(15 - y_{h2})}{30}\pi - \pi \tag{4}$$

This mapping allowed the y-positions of the handles to be converted into joint angles within their respective ranges, resulting in the reachable workspace shown in black in Fig. 1E. Differentiating Equations (3) and (4) yields a mapping between the handles' y-velocities and the corresponding joint angular velocities:

$$\begin{bmatrix} \dot{\theta}_1 \\ \dot{\theta}_2 \end{bmatrix} = -\frac{\pi}{30} \begin{bmatrix} \dot{y}_{h1} \\ \dot{y}_{h2} \end{bmatrix} \tag{5}$$

Simulating Forward Kinematics

Forward kinematics of the 2D arm is required to compute the endpoint position and to determine and display the arm configuration. The simulated arm link lengths l_1 and l_2, were both 12 cm. Using trigonometric analysis (Fig. 1C), the positions of the elbow and end–effector in Cartesian coordinates can be expressed using the following matrix equations:

$$\begin{bmatrix} x_{elbow} \\ y_{elbow} \end{bmatrix} = \begin{bmatrix} l_1 \cos(\theta_1) \\ l_1 \sin(\theta_1) \end{bmatrix} + \begin{bmatrix} x_{shoulder} \\ y_{shoulder} \end{bmatrix} \tag{6}$$

$$\begin{bmatrix} x_{end} \\ y_{end} \end{bmatrix} = \begin{bmatrix} l_1 \cos(\theta_1) + l_2 \cos(\theta_1 + \theta_2) \\ l_1 \sin(\theta_1) + l_2 \sin(\theta_1 + \theta_2) \end{bmatrix} + \begin{bmatrix} x_{shoulder} \\ y_{shoulder} \end{bmatrix} \tag{7}$$

Differential kinematics of the 2D arm are required to relate handle velocities to endpoint velocities and to map endpoint forces back to forces at the vBOT handles. The Jacobian matrix of the 2D arm is given by:

$$J = \begin{bmatrix} \frac{\partial x_{end}}{\partial \theta_1} & \frac{\partial x_{end}}{\partial \theta_2} \\ \frac{\partial y_{end}}{\partial \theta_1} & \frac{\partial y_{end}}{\partial \theta_2} \end{bmatrix} = \begin{bmatrix} -l_1 \sin(\theta_1) - l_2 \sin(\theta_1 + \theta_2) & -l_2 \sin(\theta_1 + \theta_2) \\ l_1 \cos(\theta_1) + l_2 \cos(\theta_1 + \theta_2) & l_2 \cos(\theta_1 + \theta_2) \end{bmatrix} \tag{8}$$

The relationship between the handle velocities and the extrinsic endpoint velocity is given by the following expression:

$$\begin{bmatrix} \dot{x}_{end} \\ \dot{y}_{end} \end{bmatrix} = J \begin{bmatrix} \dot{\theta}_1 \\ \dot{\theta}_2 \end{bmatrix} = -\frac{\pi}{30} J \begin{bmatrix} \dot{y}_{h1} \\ \dot{y}_{h2} \end{bmatrix} \tag{9}$$

Task Force Feedback

Although the arm itself was modeled as a purely kinematic structure with no intrinsic dynamics, different endpoint dynamics were simulated by mapping loads applied at the endpoint back to the y-direction forces experienced by the participants at the control handles. The relationship between the virtual arm endpoint force vector $[F_{xend} \quad F_{yend}]^T$ and the joint torque vector $[\tau_1 \quad \tau_2]^T$ is given by:

$$\begin{bmatrix} \tau_1 \\ \tau_2 \end{bmatrix} = J^T \begin{bmatrix} F_{xend} \\ F_{yend} \end{bmatrix} \tag{10}$$

Where J^T is the transpose of the arm's Jacobian matrix. The torques $[\tau_1 \quad \tau_2]^T$ at the arm joints were mapped to corresponding y-direction forces, $[F_{h1} \quad F_{h2}]^T$, applied at the vBOT handles by accounting for the mechanical advantage relating handle displacement to joint rotational angles. This mapping yields the following conversion formula:

$$\begin{bmatrix} F_{h1} \\ F_{h2} \end{bmatrix} = dir_{slider} \frac{(\theta_{max} - \theta_{min})}{\text{chanLen}} \begin{bmatrix} \tau_1 \\ \tau_2 \end{bmatrix} \tag{11}$$

Substituting the expression for the joint torques and the corresponding numerical values yields the final expression for the force along the y-axis at the handle in terms of endpoint force:

$$\begin{bmatrix} F_{h1} \\ F_{h2} \end{bmatrix} = -\frac{\pi}{30} J^T \begin{bmatrix} F_{xend} \\ F_{yend} \end{bmatrix} \tag{12}$$

Endpoint Dynamics Simulation

In the null-field condition, when the arm endpoint was unloaded, no endpoint forces were generated or experienced at the control handles during arm movement. When endpoint dynamics were introduced, namely, a viscous curl-field, an added mass, or a combination of both, resulting endpoint forces were mapped back to the handles and perceived by participants as they moved the arm through the workspace.

Endpoint Curl-field Simulation

In curl-field endpoint trials, a velocity-dependent curl-field [12] was implemented by relating arm endpoint velocity to the endpoint force:

$$\begin{bmatrix} F_{xend} \\ F_{yend} \end{bmatrix} = b_{curl} \begin{bmatrix} 0 & -1 \\ 1 & 0 \end{bmatrix} \begin{bmatrix} \dot{x}_{end} \\ \dot{y}_{end} \end{bmatrix} \tag{13}$$

The curl-field constant b_{curl} was set to ±16 N.s.m^{-1}, where the sign determined the direction of the curl-field (clockwise or counterclockwise). In each experiment, the curl-field direction was counterbalanced across the eight participants to minimize directional bias. Each participant experienced only one curl-field direction.

The endpoint velocity used in Equation (13) was calculated from the handle velocities using Equation (9). The corresponding forces experienced along the y-direction at the handles were then calculated using Equation (12). The total two-dimensional force applied to the vBOT handles was computed as the sum of the channel force component and the force feedback component arising from the effect from the curl-field.

Simulating Endpoint Mass

To achieve a stable simulation, a moving mass was modeled as being connected to the endpoint of the virtual arm by a strong spring. Viscous damping was also included in the simulation to improve stability. At the start of the simulation, the spring was set to its rest length, and the mass position was initialized to coincide with the current endpoint of the arm. The mass velocity and initial acceleration were set to zero, and the force acting on the mass was initialized to zero. In the main vBOT simulation update loop, running at the nominal frequency of 1 kHz, the real-time simulation of the arm and endpoint mass was executed. At each time step, mass position was updated using forward Euler integration:

$$\begin{bmatrix} x_m \\ y_m \end{bmatrix} = \begin{bmatrix} x_m \\ y_m \end{bmatrix} + \begin{bmatrix} v_{xm} \\ v_{ym} \end{bmatrix} \Delta t \tag{14}$$

Where Δt is the timestep since the previous update (nominally 1 ms). We then estimated the acceleration of the mass using the equation:

$$\begin{bmatrix} a_{mx} \\ a_{my} \end{bmatrix} = \frac{1}{m} \begin{bmatrix} F_{xm} \\ F_{ym} \end{bmatrix} \tag{15}$$

Where m is the mass at the endpoint load (2 kg) and $[F_{xm} \quad F_{ym}]^T$ is the force acting on the mass. We used Euler integration of the acceleration of the mass to calculate endpoint mass velocity

$$\begin{bmatrix} v_{xm} \\ v_{ym} \end{bmatrix} = \begin{bmatrix} v_{xm} \\ v_{ym} \end{bmatrix} + \begin{bmatrix} a_{xm} \\ a_{ym} \end{bmatrix} \Delta t \tag{16}$$

The force acting on the mass was then computed from extension of the spring, with spring constant k_{mass} = 2000 N.m^{-1}, connecting the endpoint mass to the endpoint of the arm:

$$\begin{bmatrix} F_{xm} \\ F_{ym} \end{bmatrix} = -k_{mass} \left(\begin{bmatrix} x_m \\ y_m \end{bmatrix} - \begin{bmatrix} x_{end} \\ y_{end} \end{bmatrix} \right) \tag{17}$$

An additional viscous damping term was applied to the endpoint to improve stability:

$$\begin{bmatrix} F_{xdamp} \\ F_{ydamp} \end{bmatrix} = -b_{end} \begin{bmatrix} \dot{x}_{end} \\ \dot{y}_{end} \end{bmatrix} \tag{18}$$

Where damping viscosity b_{end} = 10 N.s.m^{-1}. The mass force (Equation 17) and damping force (Equation 18) were summed, and the corresponding forces experienced in the y-direction at the handles were then calculated using Equation (12). Again, the total two-dimensional force applied to the vBOT handles corresponded to the sum of the channel force component and the endpoint force-feedback endpoint components.

Simultaneous Endpoint Mass and Curl-field

In trials with both an endpoint mass and a curl-field present, we first computed the endpoint mass and curl-field components as described previously. The vBOT applied an overall two-dimensional force to its handles by summing the force-feedback components from the curl-field and the endpoint mass, together with the channel forces that restrict handle movement to the y-direction.

Experimental Protocol

Participants executed center-out and out-back reaching movements with the endpoint of the two-dimensional (2D) planar arm. Each center-out movement began at a central 'home' position (radius: 1.0 cm; pink) and ended at one of eight peripheral targets, randomly selected without replacement (radius: 1.0 cm, pink), evenly spaced 0°, 45°, 90°, 135°, 180°, 225°, 270°, and 315° on a circle of 10 cm radius centered at (0, 0). The home start position was in the mid-sagittal plane, approximately 30 cm below eye level and 30 cm anterior to the participant's chest. Each center-out movement was followed by an out-back movement, which involved reaching back from the previous center-out target to the central home start position.

At the beginning of each trial, the manipulanda automatically positioned the handles so the endpoint of the virtual arm was at the home location. Participants were required to keep the cursor within the central starting position and maintain cursor speed below 0.1 cm/s. After a 0.5 s delay, a target appeared at a location randomly selected without replacement, the arm became visible, and a tone indicated that the participant should move out to the target.

Each block comprised 17 trials: 8 outward (center-out) and 8 inward (out-back) movements with the simulated arm visible. In addition, one outward movement was performed with the arm invisible. The outward movements constituted a typical center-out task, enabling comparison of behaviors with other such studies in the literature. The inward (out-back) movement provided further coverage of the operating space using movements in the opposite direction. A trial terminated when the cursor was within 0.5 cm of the target and cursor speed dropped below 0.01 cm/s.

An outward catch-trial movement to a randomly selected target from one of the four cardinal directions (0°, 90°, 180°, or 270°) was also included in each block of 17 trials. In this catch trial, both the arm and the endpoint cursor were invisible, allowing assessment of feedforward control. Since catch trials are made without visual indication of cursor position, trial termination occurred when cursor speed fell below 0.01 cm/s. This criterion was used because accurate movement to a catch target was difficult and was often not achieved.

Participants were instructed to move the cursor into the target as quickly as possible and to remain stationary once the target was reached. However, participants were not instructed to move at a prescribed speed. This design choice was intentional, as movement duration and velocity are known to be emergent properties of motor learning, reflecting evolving control strategies rather than independent task variables. Participants were required to complete a trial movement within 10 s; otherwise, the trial was aborted. During each trial, handle positions and velocities, as well as the virtual arm's endpoint position and velocity, were recorded.

Experiments

We conducted two independent experiments, each comprising eight different participants, to investigate the learning and control of a virtual planar (2D) arm. Each participant completed two sessions of 2,380 trials conducted on separate days (see Fig. 1H). We did not implement a familiarization period in which trial data were excluded, as we aimed to minimize the overall length of the experimental session and because initial behavior itself provides meaningful insight into participant's movement strategies and performance.

Kinematic Arm Task Experiment 1.

This experiment examined de novo acquisition of kinematic control of a two-dimensional arm operating without an endpoint mass. On Day 1, participants executed point-to-point reaching movements in a null-field environment.

Day 2 began with a brief re-exposure to the null field, comprising the first 20% of trials (n = 476), to re-establish baseline performance. A velocity-dependent viscous curl-field was then imposed for the majority of the session (n = 1,870). The resulting endpoint forces were computed as joint torques via the Jacobian transpose and subsequently transformed into linear forces at the handles, enabling participants to perceive the perturbation. In the final two blocks (n = 34 trials), the curl-field was removed to assess washout after-effects following prior dynamic exposure.

Endpoint Mass Arm Task Experiment 2.

Experiment 2 was similar to Experiment 1, but introduced a dynamically coupled 2 kg endpoint mass, implemented via a spring–mass–damper system that generated state-dependent forces during movement. The actuation forces generated by motion of the mass were first related to the virtual arm joint torques and subsequently mapped to corresponding forces at the control handles. Participants were not informed about the nature of the endpoint dynamics, and the endpoint-mass condition was designed to provide state-dependent forces related primarily to movement acceleration, rather than velocity-dependent perturbations.

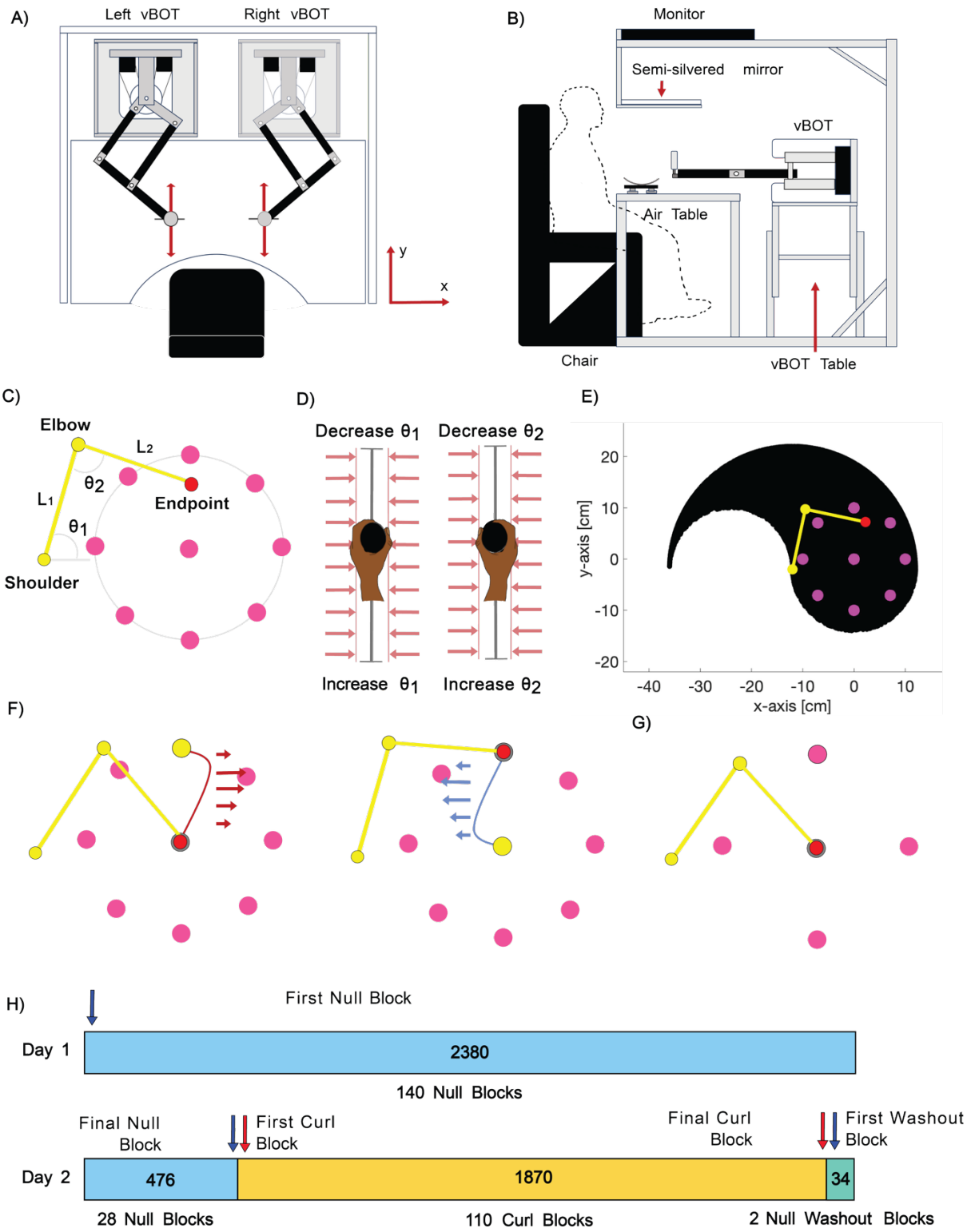

Figure 1. Experimental Setup and Task Design. **A:** Control of a virtual two-dimensional (2D) arm was conducted using the vBOT robotic manipulandum. **B:** The left and right handle y-positions determine the arm joint angles. The handles are constrained to linear channels. **C:** Schematic plan view of the simulated planar two-joint revolute arm. The lower link has a length L_1, and the upper link has a length L_2. The position of the end–effector is affected by both link angles θ_1 and θ_2. **D:** Angles θ_1

and θ_2 are controlled by moving the robotic handles in two separate channel trials. Moving the left handle (controlling θ_1) up decreases the angle, while moving it down increases the angle. Similarly, moving the right handle (controlling θ_2) up decreases the angle, and moving it down increases it. **E:** The robotic arm's reachable workspace is shown in black, illustrating the reachability of the virtual arm endpoint when driven by the bimanual control positions. The center-out and out-back task, home position, and targets fit within the workspace. **F:** Curl-field trials. Participants performed outward and inward movements toward a displayed yellow target. After completing null-field training, they were exposed to two distinct directional curl-fields. Half of the participants experienced clockwise (CW) curl-fields during outward movements and inward movements. The other half experienced counterclockwise (CCW) curl-fields during outward and inward movements. This design counterbalanced the exposure to each field type across participants. **G:** Channel trials. These only used a single adaptation movement direction to a target point (0°, 90°, 180°, or 270°). **H:** Training and testing trial schedule for the experiment. Each block contains 17 trials: eight cursor-visible center-out movements to a target, 8 cursor-visible out-back movements to the home position, and 1 invisible-cursor center-out catch movement to one of four targets. Location of informative trajectory observation points included: First Null Block, Final Null Block, First Curl Block, Final Curl Block, and First Washout Block.

Data Analysis

The experimental data were processed offline using MATLAB R2024a.

Hand Trajectory Plots

Hand trajectory plots provide an intuitive visualization of participants' movement behavior throughout the experiment. They illustrate naïve control early in training, the progressive refinement that accompanies exposure to external dynamics (e.g., viscous curl-fields), and the re-emergence of baseline patterns once those forces are removed, thereby revealing learning, adaptation, and de-adaptation within a single visualization.

In both experiments, several key phases are critical to understanding participants' motor performance and adaptation. These include the first and final blocks of null-field trials (baseline establishment and improvement), the first and final blocks of curl-field exposure (early and late adaptation), and the first washout block (de-adaptation).

Hand trajectory plots allow direct comparison of movements during outward and inward paths and provide insight into both extrinsic trajectories (endpoint-space paths) and intrinsic trajectories (joint space paths). Additionally, catch trials, in which the target is shown but no visual feedback of the arm is provided, are included to assess

the development of feedforward predictive control used to manipulate the novel structure of the 2D arm.

Trajectory quantification: Several measures were calculated to quantify the movement trajectory of each individual trial. First, the movement start and end points were determined in both time and space. A movement was considered to have started when the center of the extrinsic cursor left the center of the starting target circle (radius: 0.5 cm) and was traveling at a speed greater than 0.01 cm/s. A movement was considered to have stopped when the center of the extrinsic cursor reached the extrinsic target circle (radius: 0.5 cm). For catch trials, in which the cursor was invisible, movement termination was instead defined by cursor speed falling below the threshold.

Movement Speed and Duration

Movement duration and peak speed were analyzed as dependent variables rather than controlled parameters. This approach is consistent with prior work on de novo learning, where changes in speed reflect the stabilization of control policies. To ensure that group differences in adaptation were not trivially driven by speed, we also performed analyses that normalized deviation metrics by peak movement speed (see Results).

Performance Metrics for Visible Movements

We quantified the kinematic accuracy of visible movements with four complementary deviation metrics.

Extrinsic Signed Maximum Perpendicular Error (SMPE): We calculated the signed maximum deviation of the 2D arm endpoint trajectory from a straight-line path connecting the starting cursor location and the target cursor location in extrinsic space. This measure preserved the direction of the maximum deviation from a straight-line trajectory. Consequently, the effects of random fluctuations were minimized, since contributions from positive and negative deviations cancel out in the averaging procedure. As a result, the group-mean SMPE is a clearer indicator of systematic bias in the trajectories. Accordingly, since its introduction, this has been the preferred metric used to assess deviation from a straight line in curl-field adaptation experiments [38].

Adaptation to the curl-field was primarily assessed using signed maximum perpendicular error (SMPE), which captures systematic directional bias and is the standard metric for predictive compensation in force-field learning. Unlike unsigned measures of curvature, SMPE distinguishes predictive compensation from passive mechanical effects and is therefore central to interpreting adaptation.

Speed-normalized curl-field analysis (SMPEN): To ensure that differences in experienced force magnitude did not trivially account for group differences, SMPE and trajectory deviation metrics were normalized by peak movement speed.

Extrinsic Absolute Maximum Perpendicular Error (AMPE): For each trial, we took the absolute value of the maximum perpendicular deviation of the 2D arm endpoint trajectory from the ideal straight-line path joining the start cursor location and the target cursor location in extrinsic space. This measure ensures that positive and negative deviations over trials do not cancel out and gives an overall indication of how well participants were able to move along a straight trajectory from the starting point to the target, making it a suitable metric to quantify overall control of the virtual arm.

Movement Duration: The difference between movement onset and termination times.

Movement Length: To estimate the extrinsic movement path length, we computed the sum of the distances between adjacent (x, y) cursor trajectory positions, calculated using the Pythagorean theorem, from the start to the end of the movement trajectory.

Mean ± SE over Trials and Participants

The average values of each trajectory metric were first computed across all trials within a given set of blocks. The mean ± standard error (SE) of the resulting average values was then calculated across all participants.

Performance Metrics for Catch Movements

Catch trials were used to assess predictive control of the learned mapping in the absence of visual feedback. Because no online visual correction was possible and trials terminated based on movement cessation rather than target acquisition, catch-trial performance reflects feedforward movement planning under uncertainty about the endpoint location. Catch-trial performance was quantified using two complementary termination-based metrics.

Trial-end distance from start: The Euclidean distance between the start location and the endpoint at movement termination, defined by cursor speed falling below the threshold, was calculated.

Trial-end distance from target: The Euclidean distance between the target location and the endpoint at movement termination was calculated.

Learning-curve Analysis

Learning-curve analyses were restricted to SMPE during curl-field exposure, as unsigned error metrics such as AMPE do not selectively reflect predictive compensation and can decrease through non-adaptive strategies such as co-contraction. Learning dynamics were quantified by fitting an exponential model to trial-by-trial performance,

$$y(t) = Ae^{-t/\tau} + C \tag{19}$$

where A is the initial error amplitude, τ is the learning time constant, and C is the asymptotic performance level. Model fits were performed both on pooled trial data within each condition and at the individual-participant level.

To assess differences between conditions, group-level parameter differences were evaluated using a participant-level permutation test. Participants from both conditions were pooled and repeatedly reassigned to two pseudo-groups of equal size without replacement, preserving the original group sizes. For each permutation, the exponential model was refitted to the pooled trial data within each pseudo-group and parameter differences were computed. Two-sided p-values were calculated as the proportion of permuted parameter differences whose absolute magnitude exceeded that of the observed difference. Exact permutation testing was used where feasible; otherwise, p-values were estimated from a large number of random permutations. Participant-level learning-rate estimates were additionally compared using Welch's two-sample t-tests. Statistical significance was assessed at $\alpha = 0.05$.

Statistics

Statistical analyses were conducted in JASP [39]. A Mauchly's test of sphericity was applied to check for sphericity wherever applicable. In cases where the Mauchly's test was significant, the degrees of freedom were adjusted using a Greenhouse-Geisser correction. The α-level was set to 0.05 in all tests. We report omega squared as the effect size (ω^2).

Each of the two experiments was conducted with different participants, resulting in a total of two sets of SMPE, AMPE, path length, and movement duration data. For each of these two datasets in isolation, we first performed repeated measures ANOVAs to examine differences in SMPE, AMPE, path length, and duration data at various critical phases within each experimental condition. We also similarly analyzed SMPEN, the speed-normalized measure.

To evaluate these metrics within each experimental condition, we compared the mean of each metric over two blocks for the initial null phase, the final null phase, the initial

curl-field exposure phase, the final curl-field exposure phase, and the washout phase. This comparison was conducted using a repeated-measures ANOVA, with phase as a repeated-measures factor (five levels). When a significant main effect was observed, we proceeded with post-hoc comparisons using the Holm-Bonferroni correction.

To compare results across experiments for the metrics, we analyzed the mean of each metric over ten blocks using an ANOVA across the final null phase, the initial curl-field exposure phase, and the final curl-field exposure phase. In this analysis, experimental condition (two levels) was considered the factor. Post-hoc comparisons were conducted with the Holm-Bonferroni correction if a significant main effect was detected.

Results

The Kinematic Arm Task Experiment 1 involved first learning how to control a virtual revolute arm using a purely arbitrary kinematic mapping between hand movements and joint angles. It then investigated the effect of an endpoint curl-field. Each participant performed two sets of 2,380 trials, with each conducted on a separate day. On Day 1, the arm was controlled with a purely kinematic mapping from hand positions to joint angles. On Day 2, the first 20% of trials retained this kinematic mapping. For the remainder, the endpoint was simulated to move through a viscous curl-field and participants experienced corresponding joint torques as reaction forces at their hands.

We recorded and subsequently analyzed participants' behavior as they learned the novel kinematics and dynamics of the simulated 2D arm. This process was undertaken for both experiments, Experiment 1 – Kinematic Arm Task and Experiment 2 – Endpoint Mass Task. See Fig. 1H for the location of informative phases in the experiments discussed below.

Trajectory Plots Kinematic Arm Task Experiment 1

We first examined representative hand trajectories during the initial null phase for a single participant. Fig. 2A shows the extrinsic and intrinsic outward-movement trajectories for the first null block for a typical participant. The extrinsic paths were highly erratic as participants searched for the target location, and the corresponding intrinsic movement trajectories showed segmented, independent hand movements that are typical of early learning. By the final null block, the participant exhibited straighter extrinsic paths, as shown in Fig. 2B. The previously independent hand movements were replaced by simultaneous and continuous intrinsic motions.

We then examined outward movement trajectory trends across participants. Fig. 2C plots the mean ± SE extrinsic trajectories across participants in the clockwise (CW)

condition, and Fig. 2D shows the corresponding trajectories in the counterclockwise (CCW) condition. In the initial null block, trajectories deviated substantially from straight-line paths. However, by the end of the null phase, their outward paths to the targets became consistently straighter. Upon introducing a curl-field, participants' trajectories became systematically curved, as the curl-field pushed them away from their straight paths. By the end of the curl-field exposure phase, participants exhibited adaptation, straightening their hand trajectories. This adaptation process resembles typical curl-field adaptation. In the final washout phase, the curl-field was removed, and pronounced after-effects were observed. These after-effects manifested as deviations from the intended path in the direction opposite to the original curl-field force.

We examined the mean ± SE speed profiles across all extrinsic movements over the same experimental phases, as shown in Fig. 2E. Initially, movements were slow and exhibited a uniformly low speed across the movement trajectory. By the end of the null phase, the speed profile more closely resembled that of a minimum-jerk extrinsic point-to-point movement, exhibiting a characteristic peak. However, there was still some asymmetry in the speed profile. The introduction of the curl-field slowed down the movements and skewed the profile toward lower speeds initially, although the shape of the speed profile became more symmetric and increased in peak speed by the end of adaptation to the curl-fields. In the washout phase, the after-effect led to a more variable speed profile.

Catch trials, performed without visual feedback, assessed feedforward control of the virtual arm. We examined the catch trial trajectories made by participants at the start of the experiment, at the end of the null exposure phase, and at the end of curl-field exposure. The raw trajectories are presented in Fig. 2F, as each participant behaved differently, and average plots would obscure their individual characteristics. Initially, the movements were often made in inappropriate directions and of inappropriate length. By the end of the null training, movement directions and lengths had improved, although substantial inaccuracy in most of the trajectories. At the end of curl-field training, by which time participants had the most experience learning to control the virtual arm, the directions and lengths of the catch movements had improved further.

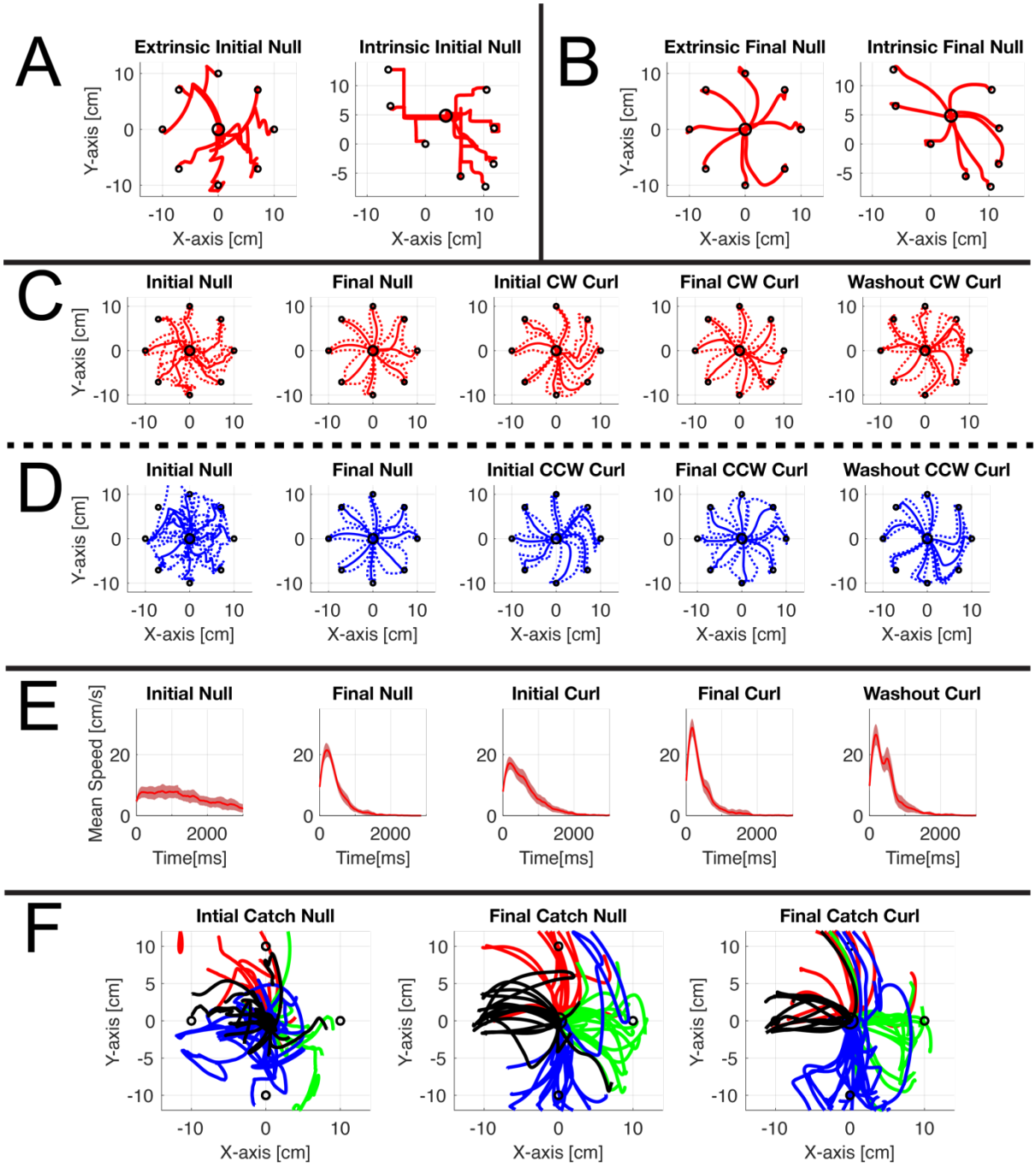

Figure 2. Trajectory plots for Experiment 1 – Kinematic Arm Task. **A:** Representative extrinsic and intrinsic trajectories from the first null block of an individual participant. **B:** Representative extrinsic and intrinsic trajectories from the final null block of the same participant. **C:** Mean ± SE extrinsic outward trajectory paths for the clockwise (CW) curl-field condition during the initial null block, final null block, initial curl block, final curl block, and washout blocks. **D:** Corresponding mean ± SE extrinsic outward trajectory paths for the counterclockwise (CCW) curl-field condition. **E:** Corresponding mean ± SE extrinsic speed profiles collapsed across CW and CCW trials. **F:** Extrinsic catch-trial trajectories from the first 8 null blocks, the final eight null blocks, and the final eight curl blocks. Trajectories to the 0°, 90°, 180°, and 270° targets are plotted in red, green, blue, and black, respectively.

Trajectory Plots Endpoint Mass Task Experiment 2

Fig. 3 shows trajectory plots from Experiment 2 (Endpoint Mass Task), which closely parallel those in Figure 2 from Experiment 1 (Kinematic Arm Task).

Fig. 3A displays the outward extrinsic and intrinsic trajectories during the initial null phase for a typical participant. As in Experiment 1, extrinsic paths were initially erratic, whereas intrinsic movements showed segmented, independent control of the two inputs.

Fig. 3B shows the final null block, where extrinsic trajectories became straighter and intrinsic hand movements became continuous and coordinated.

Fig. 3C and Fig. 3D show the mean ± SE extrinsic outward trajectories across participants in the clockwise (CW) and counterclockwise (CCW) conditions, respectively. Movements initially deviated significantly from the straight-line paths but straightened by the end of the null phase. Introduction of the curl-field led to systematic curvature, which diminished with adaptation. Upon washout, typical after-effects emerged, showing curvature in the direction opposite to the field direction.

Fig. 3E presents mean ± SE speed profiles for extrinsic movements. Early movements were slow with flat-topped profiles; by the end of the null phase, a clear single peak resembling a minimum-jerk profile emerged, though still somewhat asymmetric. The curl-field initially reduced peak speed and skewed the profile, but symmetry and peak velocity improved by the end of exposure. Washout produced more variable speed profiles.

Fig. 3F shows catch trial trajectories from individual participants at the start, end of null training, and end of curl-field training. As in Experiment 1, early catch movements were often misdirected or poorly scaled. With training, both direction and movement length improved, reflecting improved feedforward control of the virtual arm.

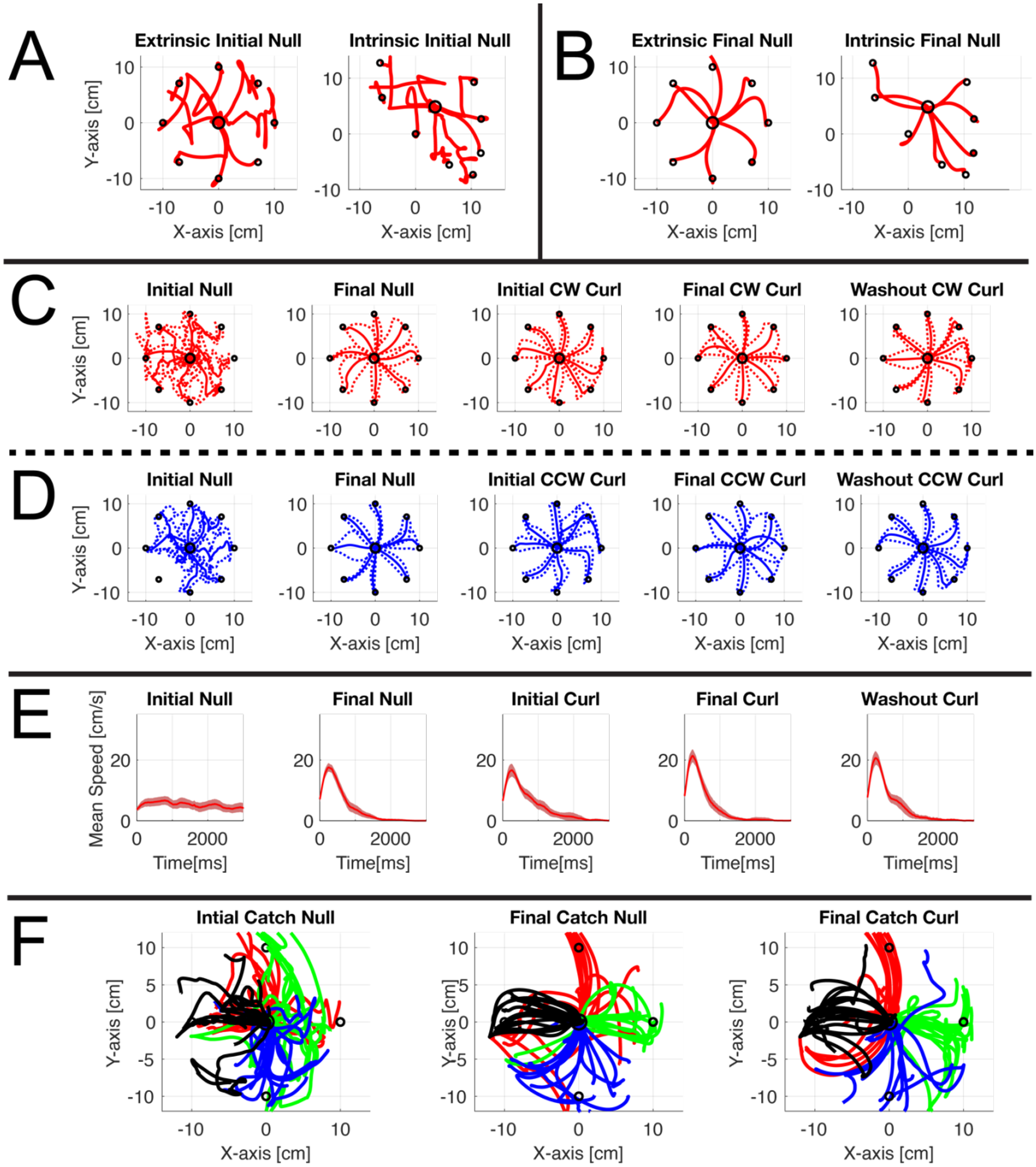

Figure 3. Trajectory plots for Experiment 2 – Endpoint Mass Task. **A:** Representative extrinsic and intrinsic trajectories from the first null block of an individual participant. **B:** Representative extrinsic and intrinsic trajectories from the final null block of the same participant. **C:** Mean ± SE extrinsic outward path trajectories for the CW curl-field condition. **D:** Mean ± SE extrinsic outward path trajectories for the CCW curl-field condition. **E:** Mean ± SE extrinsic speed profiles across CW and CCW trials. **F:** Extrinsic catch-trial trajectories for the first eight null blocks, the final eight null blocks, and the final 8 curl blocks. Trajectories to the 0°, 90°, 180°, and 270° targets are plotted in red, green, blue, and black, respectively.

Examining Effects within Experiments

We quantified movement trajectory quality with four metrics, SMPE, AMPE, movement duration, and path length, first averaging values across pairs of trial blocks (32 trials per pair). The mean ± SE values of each metric across participants are plotted in Fig. 4. Since the experiments ran over two separate sessions, we noted a slight discontinuity in metrics at the start of the second session.

To check for significance within each experimental condition, we compared the metrics at five critical stages: at the start of the experiment (initial null phase), at the end of the arm control training phase (final null phase), at the onset of curl-field exposure (initial curl phase), at the end of curl-field exposure (final curl phase), and finally during the curl-field washout (washout phase).

Washout analysis provided additional evidence for predictive adaptation. Following removal of the curl-field, participants exhibited systematic after-effects characterized by signed deviations in the opposite direction to the imposed perturbation. These after-effects were quantified using signed maximum perpendicular error (SMPE) over the first five washout trials. The presence of after-effects and systematic signed error reduction indicates a substantial contribution of predictive compensation, rather than passive mechanical attenuation alone.

Movement Metrics Plots Experiment 1

The SMPE values are plotted in Fig. 4A in blue. Repeated measures ANOVAs indicated that SMPE showed significant variations between the initial null, final null, initial curl, final curl, and washout phases. The data at these critical stages are also shown in bar-graph form in Fig. 5C.

Post-hoc comparisons further tested the significant differences between these phases. In the experimental condition ($F = 26.061$; $p < 0.001$; $\omega^2 = 0.617$), SMPE was highest at the initial null phase, but did not significantly decrease by the final null phase ($p_{bonf} = 1.000$). Upon introduction of the curl-field in the initial curl phase, it significantly increased ($p_{bonf} < 0.001$). By the final curl phase, SMPE significantly decreased in a fashion typical of that seen in standard curl-field exposure experiments (pbonf = 0.049). SMPE at the washout phase showed a significant difference compared to the final curl phase (pbonf = 0.002).

The AMPE values are plotted in Fig. 4B in blue. Repeated measures ANOVAs indicated that AMPE showed significant variations between the initial null, final null, initial curl, final curl, and washout phases. Post-hoc comparisons further tested the significant differences between these phases.

In this experimental condition ($F = 11.366$; $p < 0.001$; $\omega^2 = 0.463$), AMPE was high at the initial null phase, but it was significantly reduced by the final null phase (p_{bonf} =

0.027). Upon introduction of the curl-field in the initial curl phase, it significantly increased ($p_{bonf} < 0.001$). By the final curl phase, AMPE significantly decreased ($p_{bonf} = 0.043$). At the washout phase, AMPE showed a significant difference relative to the final curl phase ($p_{bonf} = 0.047$).

The movement duration is plotted in Fig. 4C in blue. Repeated measures ANOVAs indicated that movement duration showed significant variations between the initial null, final null, initial curl, final curl, and washout phases. Post-hoc comparisons further tested the significant differences between these phases. In the experimental condition ($F = 30.213$; $p < 0.001$; $\omega^2 = 0.728$), movement duration differed significantly across phases.

Movement duration was high at the initial null phase, but was significantly reduced by the final null phase ($p_{bonf} = 0.006$). Upon introduction of the curl-field in the initial curl phase, it significantly increased **(**$p_{bonf} = 0.009$). By the final curl phase, movement duration significantly decreased ($p_{bonf} = 0.029$). Movement duration at the washout phase showed no significant difference relative to the final curl phase ($p_{bonf} = 0.639$).

Extrinsic path length is shown in Fig. 4D in blue. Repeated measures ANOVAs indicated that path length showed significant variations between the initial null, final null, initial curl, final curl, and washout phases. Post-hoc comparisons further tested the significant differences between these phases. In the experimental condition ($F = 11.269$; $p < 0.001$; $\omega^2 = 0.466$), path length was high at the initial null phase, but it did not significantly decrease by the final null phase ($p_{bonf} = 0.061$). Upon introduction of the curl-field in the initial curl phase**,** it significantly increased ($p_{bonf} < 0.001$). By the final curl phase, path length significantly decreased ($p_{bonf} = 0.008$). Path length at the washout phase showed a significant difference relative to the final curl phase ($p_{bonf} = 0.044$).

Movement Metrics Plots Experiment 2

Participants in the endpoint-mass condition moved more slowly during early learning, a pattern consistent with a stabilization strategy during acquisition of a novel control policy. Similar speed reductions have been reported during the early stages of de novo learning, where accuracy and stability are prioritized over movement time.

Fig. 4A (green) plot shows the SMPE. Repeated measures ANOVAs indicated that SMPE showed significant variations between the initial null**,** final null**,** initial curl**,** final curl**,** and washout phases. The data at these critical stages are also shown in Fig. 5C.

Post-hoc comparisons further tested the significant differences between these phases. In the experimental condition ($F = 14.013$; $p < 0.001$; $\omega^2 = 0.504$), SMPE was highest at the initial null phase, but did not significantly decrease by the final null phase ($p_{bonf} = 1.000$). Upon introduction of the curl-field in the initial curl phase**,** it significantly increased ($p_{bonf} = 0.003$). By the final curl phase, SMPE significantly decreased (p_{bonf}

= 0.013). SMPE at the washout phase showed a significant difference compared to the final curl phase ($p_{bonf} < 0.001$).

Fig. 4B (green) plot shows the AMPE. Repeated measures ANOVAs indicated that AMPE showed significant variations between the initial null, final null, initial curl, final curl, and washout phases. Post-hoc comparisons further tested the significant differences between these phases. In the experimental condition ($F = 23.674$; $p < 0.001$; $\omega^2 = 0.629$), AMPE was high at the initial null phase, but it significantly reduced by the final null phase ($p_{bonf} = 0.014$). Upon introduction of the curl-field in the initial curl phase, it significantly increased ($p_{bonf} < 0.001$). By the final curl phase, AMPE significantly decreased ($p_{bonf} = 0.004$). AMPE at the washout phase showed a significant difference compared to the final curl phase ($p_{bonf} = 0.004$).

The movement duration is plotted in Fig. 4C in green. Repeated measures ANOVAs indicated that movement duration showed significant variations between the initial null, final null, initial curl, final curl, and washout phases. Post-hoc comparisons further tested the significant differences between these phases. In the experimental condition ($F = 166.581$; $p < 0.001$; $\omega^2 = 0.923$), movement duration was high at the initial null phase, but it significantly reduced by the final null phase ($p_{bonf} < 0.001$). Upon introduction of the curl-field in the initial curl phase, it significantly increased ($p_{bonf} = 0.016$). By the final curl phase, movement duration significantly decreased ($p_{bonf} < 0.001$). Movement duration at the washout phase showed a significant difference compared to the final curl phase ($p_{bonf} = 0.031$).

Fig. 4D (green) plot displays movement path length. Repeated measures ANOVAs indicated that path length showed significant variations between the initial null, final null, initial curl, final curl, and washout phases. Post-hoc comparisons further tested the significant differences between these phases. In the experimental condition ($F = 23.558$; $p < 0.001$; $\omega^2 = 0.647$), path length was high at the initial null phase, but it did significantly reduce by the final null phase ($p_{bonf} = 0.013$). Upon introduction of the curl-field in the initial curl phase, it significantly increased ($p_{bonf} < 0.001$). By the final curl phase, path length significantly decreased ($p_{bonf} = 0.009$). Path length at the washout phase showed a significant difference compared to the final curl phase ($p_{bonf} = 0.020$).

Comparison of Metrics Across Experiments

To compare the two experimental conditions, we again refer to the plot of the four metrics AMPE, SMPE, movement duration, and path length across block pairs, as shown in Fig. 4. In addition, we performed ANOVAs comparing metrics computed over 10 blocks (160 trials) at the end of the kinematic learning phase, at the onset of curl-field exposure, and at the final stage of curl-field exposure between the Kinematic Arm Experiment (Experiment 1) and the Endpoint Mass Experiment (Experiment 2). Quantitative comparisons of washout between conditions were not performed due to

the limited number of washout blocks available, which we considered insufficient for reliable statistical inference.

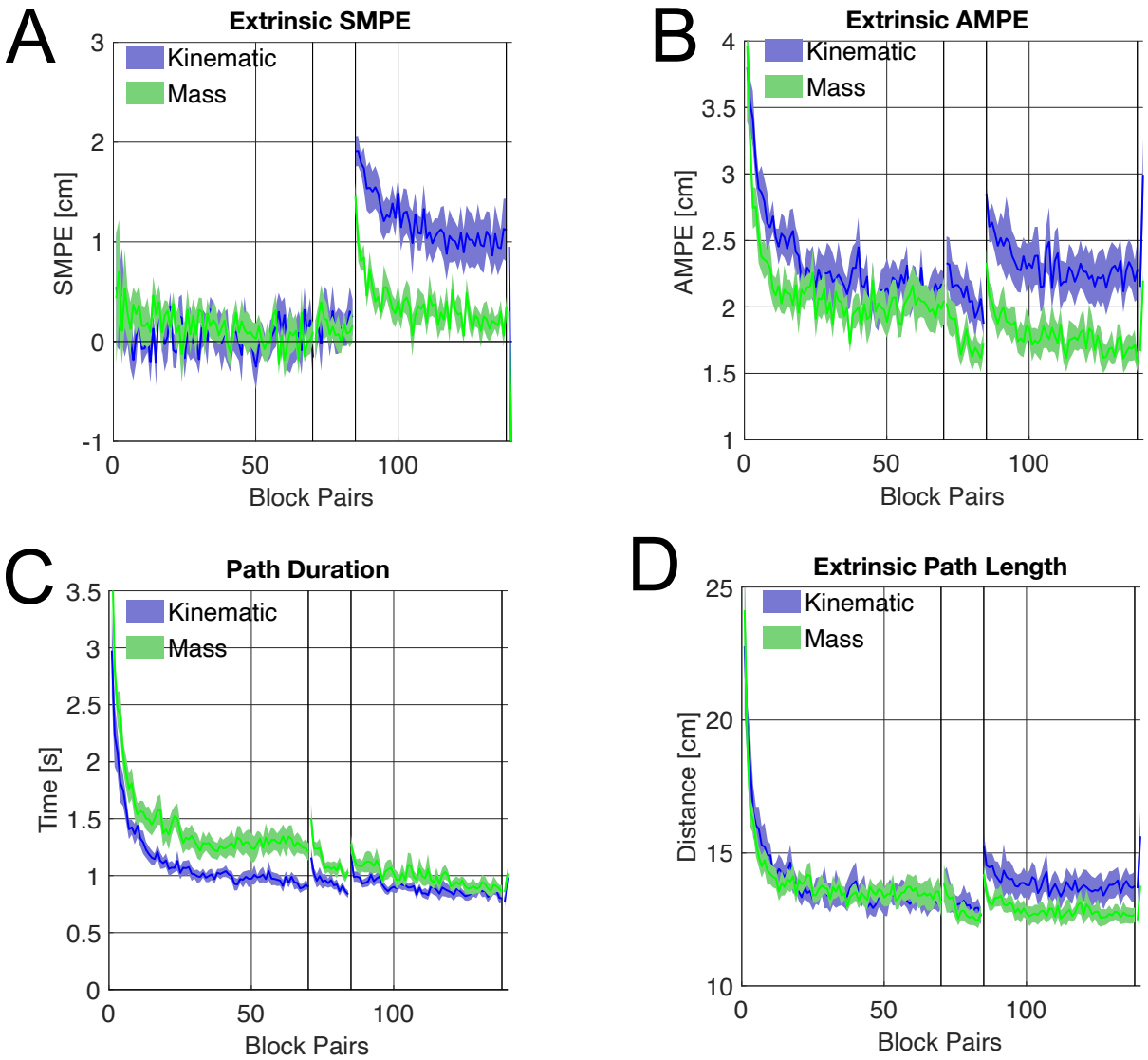

Figure 4. Comparison of movement metrics averaged over pairs of trial blocks (32 trials per point) between Experiment 1 – Kinematic Arm Task (blue) and Experiment 2 – Endpoint Mass Task (green). **A:** Mean ± SE extrinsic signed maximum perpendicular error (SMPE) over the experiments. **B:** Mean ± SE extrinsic absolute maximum perpendicular error (AMPE) shown over the experiments. **C:** Mean ± SE trial duration over the experiments. **D:** Mean ± SE extrinsic path length over the experiments.

Fig. 4A shows signed maximum perpendicular error (SMPE) plotted against pairs of trial blocks. The final null phase showed no significant difference across experimental conditions ($F = 0.176$; $p = 0.681$; $\omega^2 < 0.001$). The initial curl-field phase showed a significant difference across experimental conditions ($F = 32.405$; $p < 0.001$; $\omega^2 = 0.662$), and post-hoc comparisons confirmed this effect ($p < 0.001$). The final curl-field

phase also showed a significant difference across experimental conditions ($F = 9.015$; $p = 0.010$; $\omega^2 = 0.334$).

When no curl-field was present, the SMPE indicated minimal directional bias in movement trajectories. Consequently, in both training conditions, with and without the endpoint mass, SMPE values remained close to zero. However, upon introduction of the curl-field, SMPE increased markedly in both conditions. In the kinematic arm condition, SMPE decayed more slowly and maintained a substantial offset, whereas in the endpoint mass condition, SMPE declines more rapidly, returning closer to baseline levels. In both conditions, clear washout effects were observed, with SMPE values reversing sign, indicating that predictive compensation for the novel curl-field dynamics had been acquired.

Since curl-field forces scale linearly with movement velocity, reduced force magnitude alone would be expected to reduce unsigned trajectory curvature, without producing systematic changes in signed error or robust washout effects. However, the present results contradict this pattern. Both groups exhibited clear after-effects following curl-field removal, with signed errors reversing direction relative to baseline, indicating predictive compensation rather than passive mechanical attenuation. Moreover, washout errors decayed rapidly with continued practice, returning toward baseline within subsequent trials, consistent with the unlearning of an acquired feedforward compensation rather than the dissipation of residual forces.

Fig. 4B shows reduction in absolute maximum perpendicular error (AMPE) in both experimental conditions. The final null phase showed a significant difference across experimental conditions ($F = 4.778$; $p =0.046$; $\omega^2 = 0.191$). The initial curl-field phase showed a significant difference across experimental conditions ($F = 15.405$; $p =0.002$; $\omega^2 = 0.474$), and post-hoc comparisons confirmed this effect ($p =0.002$). The final curl-field phase likewise showed a significant variation across experimental conditions ($F = 8.492$; $p = 0.011$; $\omega^2 = 0.319$). Throughout training, the endpoint mass condition consistently exhibited lower AMPE values than those observed in the kinematic arm condition. Notably, by the end of the null-field phase, AMPE had decreased to a lower level in the mass condition. When the curl-field was introduced, AMPE rose again in both experimental conditions. However, the kinematic arm condition showed a consistently higher AMPE compared to the mass condition.

Fig. 4C shows movement duration across pairs of trial blocks for both experiments. The final null phase showed a significant difference across experimental conditions ($F = 18.603$; $p < 0.001$; $\omega^2 = 0.524$). The initial curl-field phase also showed a significant variation across experimental conditions ($F = 6.952$; $p = 0.020$; $\omega^2 = 0.271$). In contrast, the final curl-field phase showed no significant variation across experimental conditions ($F = 2.218$; $p = 0.159$; $\omega^2 = 0.071$). Overall, movement durations were

generally shorter in the kinematic arm condition, suggesting participants moved more slowly when performing the endpoint mass task.

Fig. 4D shows extrinsic trajectory length across trial block pairs for both experiments. The final null phase showed no significant variations across experimental conditions ($F = 1.171$; $p = 0.441$; $\omega^2 = 0.070$). The first curl phase showed no significant variation across experimental conditions ($F = 0.965$; $p = 0.512$; $\omega^2 < 0.001$). The final curl phase showed no significant variation across experimental conditions ($F = 0.830$; $p = 0.591$; $\omega^2 < 0.001$).

To summarize the main results, by the end of the kinematic learning phase, training with task-relevant haptic feedback (endpoint mass condition) produced significantly straighter movements, as indicated by lower AMPE values. In addition, the endpoint mass condition led to straighter movements at the onset of curl-field exposure and greater adaptation by the end of the curl-field exposure phase, as reflected in both AMPE and SMPE measures. Movement duration was significantly longer in the endpoint mass condition; however, extrinsic path length did not differ significantly between conditions.

Effect of Movement Velocity to Target on Trajectory Error

Because the magnitude of forces experienced in a velocity-dependent curl-field scales linearly with movement speed, differences in trajectory error could, in principle, arise from differences in movement velocity rather than from differences in predictive control. To address this possibility, we examined peak movement velocity toward the target and a speed-normalized trajectory error metric. Peak movement velocity differed between conditions (Fig. 5A); however, because velocity was treated as a nuisance scaling factor, it was not analyzed as a dependent variable.

After normalizing signed maximum perpendicular error (SMPE) by peak velocity, error remained lower in the endpoint-mass condition during curl-field exposure (Fig. 5B), indicating that reduced error in this group cannot be attributed to slower movements or reduced force magnitude alone. SMPEN was analyzed solely to assess the robustness of SMPE findings to speed normalization and was not treated as a primary outcome measure.

As discussed previously, examination of SMPE at critical experimental stages (Fig. 5C) revealed that both groups exhibited increased directional bias upon curl-field introduction, followed by systematic error reduction with practice. When considered qualitatively, normalized signed error (SMPEN; Fig. 5D) likewise exhibited clear washout after-effects following curl-field removal, consistent with predictive compensation rather than passive mechanical attenuation. Together, these observations confirm that prior training with task-relevant dynamics led to more

complete adaptation to the velocity-dependent perturbation, independent of movement speed.

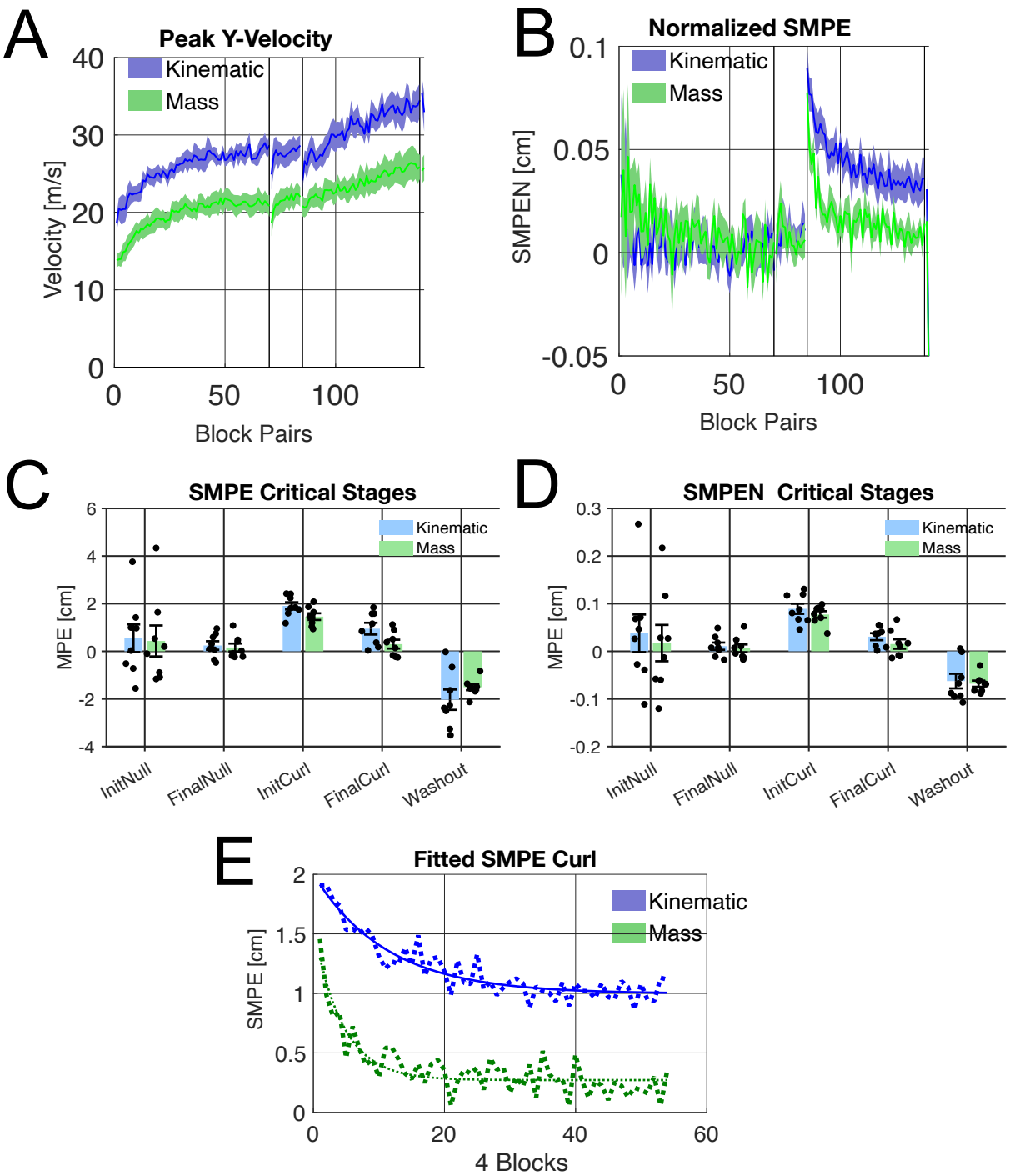

Figure 5. Examination of the effect of peak velocity. **A**: Peak velocity toward the target (mean ± SE). **B**: Signed maximum perpendicular error (SMPE) normalized by peak velocity. **C**: SMPE at critical stages of the experiment. **D**: Normalized SMPE (SMPEN) at critical stages. **E**: Exponential fits (solid lines) applied to pooled SMPE learning curves during curl-field exposure. Learning rates did not differ reliably between conditions, whereas the endpoint-mass condition exhibited a significantly lower asymptotic error, indicating more complete predictive compensation.

Analysis of Learning Time Constant

To characterize learning during curl-field exposure, an exponential model (see Methods) was fitted to SMPE learning curves derived from curl-field trials only (Fig. 5E). Group-level differences in learning parameters were assessed using a participant-level permutation test.

For the kinematic condition, the fitted group-level parameters were A = 1.0030, tau = 11.1931, and C = 0.9967. For the endpoint-mass condition, the corresponding parameters were A = 1.2853, tau = 4.3937, and C = 0.2723. Although the estimated learning time constants differed numerically between conditions, permutation testing revealed no reliable group difference in learning rate (tau; $p = 0.2415$) or in the initial amplitude parameter A ($p = 0.2859$). In contrast, the asymptotic performance parameter C differed significantly between conditions ($p = 0.0119$), indicating a difference in final predictive compensation rather than in the speed of learning.

As a robustness check, the same exponential analysis applied to speed-normalized signed error (SMPEN) yielded the same qualitative pattern of results: learning-rate parameters did not differ reliably between conditions (A and tau), whereas the asymptotic parameter C again provided the only evidence for a condition difference ($p = 0.042$).

Feedforward Control Evidence from Catch Trials

Catch trials, in which visual feedback of both the cursor and arm was removed, were used to assess feedforward control of the learned movement–outcome mapping. Because no online visual correction was possible and trial termination was based solely on movement cessation, catch-trial performance reflects predictive specification of movement extent rather than visually guided endpoint correction.

Initial catch-trial movements exhibited highly variable and inconsistent movement directions, particularly early in learning, rendering directional error measures unreliable and uninformative. Accordingly, catch-trial analysis focused on movement extent at trial termination, which provides a robust indicator of feedforward control under these conditions.

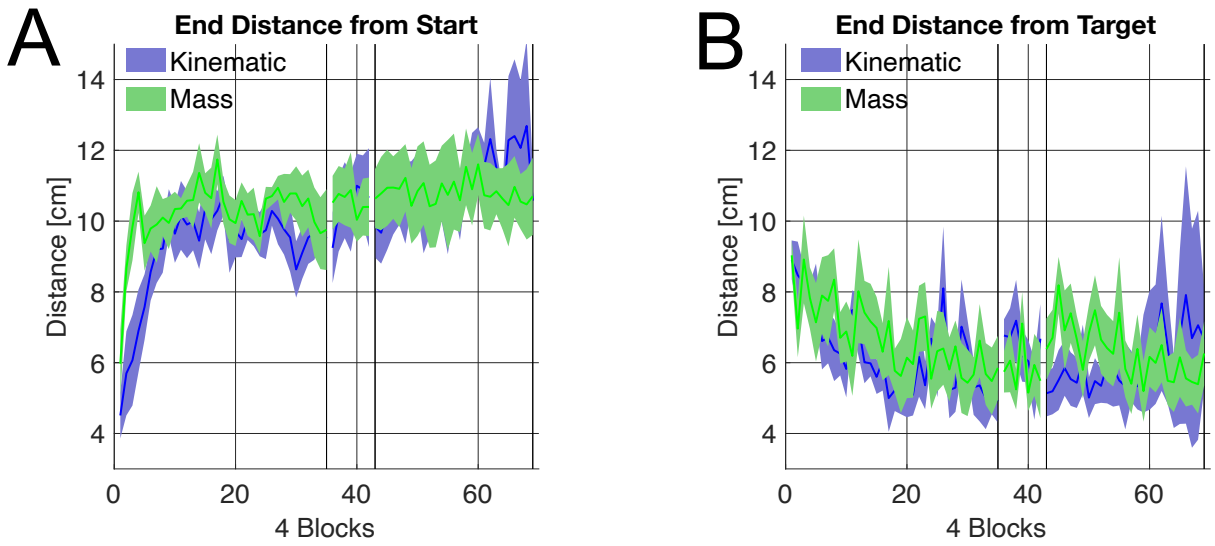

Figure 6. Examination of predictive control. **A:** Deviation from the start point at movement termination. **B:** Deviation from the target point following movement termination.

Deviation from the start point at movement termination increased systematically across training (Fig. 6A), indicating that participants progressively produced movements of greater extent rather than prematurely terminating movements. Conversely, deviation from the target point at termination decreased across training (Fig. 6B). Catch trials were included to qualitatively assess the development of feedforward control and were not subjected to formal statistical comparison due to their limited frequency.

Discussion (1258)

Summary

In this study, we examined how learning a novel movement–outcome mapping is shaped by haptic feedback and how such learning influences subsequent adaptation to unpredictable dynamics. We found that participants trained with endpoint dynamics, compared with a kinematic-only control group, showed reduced directional bias during de novo learning and stronger predictive adaptation to a later velocity-dependent curl-field, as reflected by greater reduction in signed error over training and robust washout effects. Crucially, in both conditions, the presence of robust washout after-effects indicates predictive compensation rather than passive mechanical attenuation. Together, the results indicate that prior experience with task-relevant dynamics alters how participants subsequently respond to novel velocity-dependent perturbations.

Group differences in adaptation could not be explained by movement speed alone: although movement durations differed between conditions, path length did not, and speed-normalized analyses of curl-field adaptation yielded the same pattern of results.

Catch trials (with no visual feedback of the cursor or arm) were used to qualitatively probe feedforward control of the novel mapping. Early in training, catch movements were often misdirected and poorly scaled, consistent with exploratory control. With practice, catch-trial movements became more appropriately scaled in extent and more accurate in direction, indicating improved predictive specification of movement amplitude under feedforward control. These improvements are consistent with the acquisition of a stable feedforward control mapping from bimanual hand inputs to the virtual arm state, rather than reliance on online visual error correction alone.

In the Kinematic Task (Experiment 1), participants initially moved their hands sequentially, briefly arresting one hand before advancing the other. With practice, they adopted simultaneous bimanual movements, and extrinsic trajectories progressively straightened. Upon introduction of a curl-field, trajectories initially showed pronounced curvature, but straightened with continued exposure, similar to typical behavior observed in curl-field learning. However, examination of the SMPE suggested that adaptation was incomplete by the end of the curl-field exposure, indicating residual directional bias rather than full predictive compensation for the imposed dynamics.

The Endpoint Mass Task (Experiment 2), which added a 2-kg endpoint mass, displayed parallel trends. Early movements again featured independent hand control, but the simulated inertia induced noticeable overshoot. As training progressed, participants quickly adopted simultaneous movements and gradually learned to control the arm to perform point-to-point movements, resulting in straighter extrinsic trajectories with practice. Upon introduction of the curl-field, loopy trajectories were observed, but to a markedly lesser extent than in Experiment 1, and the SMPE was considerably lower. The systematic bias seen in Experiment 1 was absent, and SMPE values had nearly returned to baseline by the end of curl-field exposure, consistent with more complete predictive adaptation to the velocity-dependent perturbation.

A potential concern is that the mere exposure to forces during the null phase may have facilitated subsequent adaptation to the curl-field. While the present design does not allow us to fully dissociate generic force exposure from learning specific dynamic structure, several features of the results argue against a trivial explanation based on force familiarity alone. The endpoint-mass forces were state-dependent and inertia-dominated, whereas the curl-field introduced velocity-dependent forces that induced systematic directional errors. Adaptation was therefore assessed using signed error and washout, both of which reflect predictive compensation rather than passive attenuation. The stronger reduction of signed error and the presence of robust after-effects in the endpoint-mass group suggest that prior learning altered how novel

dynamics were interpreted and compensated, rather than merely reducing sensitivity to perturbations.

Accordingly, prior learning in the presence of endpoint dynamics led to more robust and complete adaptation to novel perturbations, at least within the class of mappings examined here. This has important implications for the design of training protocols in rehabilitation, robotics, and skilled tool use, where incorporating force feedback could enhance robustness, generalization, and predictive control in complex or unfamiliar task environments, rather than merely accelerating learning.

An important observation is that participants were able to adapt to the velocity-dependent curl-field following acquisition of a non-veridical kinematic mapping, with no indication that prior remapping hindered dynamic learning. Although the present study did not include a veridical-control baseline, the observed learning dynamics suggest that the motor system can acquire novel dynamics within an already remapped control space. This flexibility is consistent with the view that dynamic learning operates over abstract state representations defined by task-relevant variables rather than fixed limb-centric coordinates.

We note that differences in adaptation between conditions were not driven by differences in learning rate. Although estimated learning time constants (τ) differed numerically between conditions, permutation-based inference revealed no reliable between-group difference in learning speed. Instead, the primary distinction lay in the asymptotic level of predictive compensation achieved, with participants trained under endpoint dynamics exhibiting more complete compensation for the curl-field.

Substantial inter-individual variability in τestimates was observed, consistent with prior work showing that exponential learning-rate parameters are sensitive to early-trial fluctuations and measurement noise. Together, these findings suggest that prior exposure to task-relevant dynamics altered the *endpoint* of learning rather than accelerating the learning process itself. Thus, force-based training appears to shape the quality and completeness of predictive control, rather than simply increasing the speed of adaptation.

Haptic Feedback and Networks in the Brain

Although the present study is behavioral, the observed improvements in predictive adaptation are consistent with frameworks in which haptic feedback enriches internal model formation [40]. Proprioceptive and tactile input are known to contribute to state estimation and predictive control, processes commonly associated with distributed sensorimotor networks including cerebellar and parietal circuits.

From this perspective, learning in the presence of endpoint dynamics may provide richer error signals and state information during de novo learning, without committing

to specific neural substrates. Accordingly, we do not make claims about neural implementation but rather note that the behavioral effects observed here are consistent with established models of sensorimotor learning.

De Novo Learning

The relative ease with which we can learn novel tasks, even those involving almost arbitrary kinematics and dynamics, suggests that the motor system inherently possesses the ability to perform system identification and develop adaptive control strategies. When encountering a new motor task with an unfamiliar muscle-to-movement mapping, predictive motor commands cannot initially be generated due to the absence of prior knowledge. Consequently, exploration of the muscle activity space becomes essential for learning this relationship. Notably, this situation resembles the developmental challenges faced by infants in learning goal-directed reaching [41–43], providing a useful analogue for the present novel arm task. Learning requires the ability to evaluate actions, and improvement heavily relies on visual feedback, with haptic feedback also playing a valuable role.

Motor skill acquisition [44,45] involves the improvement of movement and task performance through practice [46]. This process ranges from simple adaptation to changes in kinematics or dynamics, to the acquisition of entirely new control strategies. Early research quantified the nature of arm kinematics and dynamics [47], laying the groundwork for later studies. Subsequent studies have furthered our understanding of how the motor system learns to navigate unfamiliar environments. For instance, research on de novo learning has investigated how individuals adapt their motor skills to control and manipulate new spatial contexts [48]. In that study, participants learned to control a cursor through coordinated movements and developed a representation of Euclidean space for remapping hand movements. Training with terminal visual feedback resulted in smoother cursor trajectories and reduced unnecessary movements in non-critical degrees of freedom. Notably, continuous visual feedback accelerated the learning process.

Future Work

Future work could further dissociate general force exposure from learning specific dynamic structure by independently manipulating endpoint and velocity-dependent forces; the present study instead provides a conceptual demonstration that learning in structured dynamics shapes subsequent adaptation.

Acknowledgements

Institutional support for ISH was provided by the School of Engineering, Computing and Mathematics, University of Plymouth. LAH was supported by a studentship from

the EPSRC. We thank John Welsh for invaluable technical support, and David W. Franklin for useful scientific discussion.

Author Contributions

ISH conceived, designed, and implemented the study. LAH conducted data collection. Data analysis was carried out by ISH. The initial draft of the manuscript was written by ISH. Both authors (ISH and LAH) reviewed and edited the manuscript.

Data availability statement

Data will be made publicly available upon publication via an online repository (details will be provided upon acceptance).

Competing Interest Statement

The authors declare that they have no financial, personal, or professional interests that could be construed to have influenced this work.

References

1. Savion-Lemieux, T. & Penhune, V. B. The effects of practice and delay on motor skill learning and retention. *Exp Brain Res* **161**, 423–431 (2005).
2. Reis, J. *et al.* Noninvasive cortical stimulation enhances motor skill acquisition over multiple days through an effect on consolidation. *Proceedings of the National Academy of Sciences* **106**, 1590–1595 (2009).
3. Shmuelof, L., Krakauer, J. W. & Mazzoni, P. How is a motor skill learned? Change and invariance at the levels of task success and trajectory control. *Journal of Neurophysiology* **108**, 578–594 (2012).
4. Krakauer, J. W., Hadjiosif, A. M., Xu, J., Wong, A. L. & Haith, A. M. Motor learning. *Compr Physiol* **9**, 613–663 (2019).

5. Krakauer, J. W., Pine, Z. M., Ghilardi, M. F. & Ghez, C. Learning of visuomotor transformations for vectorial planning of reaching trajectories. *The Journal of neuroscience : the official journal of the Society for Neuroscience* **20**, 8916–8924 (2000).
6. Krakauer, J. W., Ghez, C. & Ghilardi, M. F. Adaptation to visuomotor transformations: consolidation, interference, and forgetting. *The Journal of neuroscience : the official journal of the Society for Neuroscience* **25**, 473–478 (2005).
7. Bock, O., Schneider, S. & Bloomberg, J. Conditions for interference versus facilitation during sequential sensorimotor adaptation. *Experimental Brain Research* **138**, 359–365 (2001).
8. Goedert, K. M. & Willingham, D. B. Patterns of Interference in Sequence Learning and Prism Adaptation Inconsistent With the Consolidation Hypothesis. *Learn. Mem.* **9**, 279–292 (2002).
9. Lackner, J. R. & Dizio, P. Rapid adaptation to Coriolis force perturbations of arm trajectory. *J Neurophysiol* **72**, 299–313 (1994).
10. Shadmehr, R. & Mussa-Ivaldi, F. A. Adaptive representation of dynamics during learning of a motor task. *J. Neurosci.* **14**, 3208–3224 (1994).
11. Brashers-Krug, T., Shadmehr, R. & Bizzi, E. Consolidation in human motor memory. *Nature* **382**, 252–255 (1996).
12. Gandolfo, F., Mussa-Ivaldi, F. A. & Bizzi, E. Motor learning by field approximation. *PNAS* **93**, 3843–3846 (1996).
13. Howard, I. S., Wolpert, D. M. & Franklin, D. W. The effect of contextual cues on the encoding of motor memories. *J Neurophysiol* **109**, 2632–44 (2013).
14. Sarwary, A. M. E., Stegeman, D. F., Selen, L. P. J. & Medendorp, W. P. Generalization and transfer of contextual cues in motor learning. *J Neurophysiol* **114**, 1565–1576 (2015).

15. Howard, I. S., Ingram, J. N., Franklin, D. W. & Wolpert, D. M. Gone in 0.6 seconds: the encoding of motor memories depends on recent sensorimotor States. *J Neurosci* **32**, 12756–68 (2012).
16. Howard, I. S., Franklin, S. & Franklin, D. W. Kernels of Motor Memory Formation: Temporal Generalization in Bimanual Adaptation. *J. Neurosci.* **44**, (2024).
17. Gippert, M. *et al.* Prior Movement of One Arm Facilitates Motor Adaptation in the Other. *J. Neurosci.* **43**, 4341–4351 (2023).
18. Orschiedt, J. & Franklin, D. W. Learning context shapes bimanual control strategy and generalization of novel dynamics. *PLoS Comput Biol* **19**, e1011189 (2023).
19. Nozaki, D., Kurtzer, I. & Scott, S. H. Limited transfer of learning between unimanual and bimanual skills within the same limb. *Nature Neuroscience* **9**, 1364–1366 (2006).
20. Howard, I. S., Ingram, J. N. & Wolpert, D. M. Context-dependent partitioning of motor learning in bimanual movements. *J Neurophysiol* **104**, 2082–2091 (2010).
21. Flanagan, J. R. *et al.* Composition and decomposition of internal models in motor learning under altered kinematic and dynamic environments. *The Journal of neuroscience : the official journal of the Society for Neuroscience* **19**, RC34 (1999).
22. Krakauer, J. W., Ghilardi, M. F. & Ghez, C. Independent learning of internal models for kinematic and dynamic control of reaching. *Nature Neuroscience* **2**, 1026–1031 (1999).
23. Flanagan, J. R. & Rao, A. K. Trajectory adaptation to a nonlinear visuomotor transformation: evidence of motion planning in visually perceived space. *Journal of neurophysiology* **74**, 2174–2178 (1995).
24. Lillicrap, T. P. *et al.* Adapting to inversion of the visual field: a new twist on an old problem. *Exp Brain Res* **228**, 327–339 (2013).

25. Telgen, S., Parvin, D. & Diedrichsen, J. Mirror reversal and visual rotation are learned and consolidated via separate mechanisms: recalibrating or learning de novo? *Journal of Neuroscience* **34**, 13768–13779 (2014).
26. Pouget, A., Fisher, S. & Sejnowski, T. J. Hierarchical Transformation of Space in the Visual System. in *Advances in Neural Information Processing Systems* vol. 4 (Morgan-Kaufmann, 1991).
27. Pouget, A. & Snyder, L. H. Computational approaches to sensorimotor transformations. *Nature Neuroscience* **3 Suppl**, 1192–1198 (2000).
28. Danziger*, Z., Fishbach, A. & Mussa-Ivaldi, F. A. Learning Algorithms for Human–Machine Interfaces. *IEEE Transactions on Biomedical Engineering* **56**, 1502–1511 (2009).
29. Danziger, Z. & Mussa-Ivaldi, F. A. The Influence of Visual Motion on Motor Learning. *J. Neurosci.* **32**, 9859–9869 (2012).
30. Liu, X., Mosier, K. M., Mussa-Ivaldi, F. A., Casadio, M. & Scheidt, R. A. Reorganization of Finger Coordination Patterns During Adaptation to Rotation and Scaling of a Newly Learned Sensorimotor Transformation. *Journal of Neurophysiology* **105**, 454–473 (2011).
31. Sternad, D. It's not (only) the mean that matters: variability, noise and exploration in skill learning. *Current Opinion in Behavioral Sciences* **20**, 183–195 (2018).
32. Yang, C. S., Cowan, N. J. & Haith, A. M. De novo learning versus adaptation of continuous control in a manual tracking task. *eLife* **10**, e62578 (2021).
33. Haith, A. M., Yang, C. S., Pakpoor, J. & Kita, K. De novo motor learning of a bimanual control task over multiple days of practice. *Journal of Neurophysiology* **128**, 982–993 (2022).
34. Oldfield, R. C. The assessment and analysis of handedness: The Edinburgh inventory. *Neuropsychologia* **9**, 97–113 (1971).

35. Galvin, J. E., Tolea, M. I., Rosenfeld, A. & Chrisphonte, S. The Quick Physical Activity Rating (QPAR) scale: A brief assessment of physical activity in older adults with and without cognitive impairment. *PLOS ONE* **15**, e0241641 (2020).
36. Howard, I. S., Ingram, J. N. & Wolpert, D. M. A modular planar robotic manipulandum with end-point torque control. *J Neurosci Meth* **181**, 199–211 (2009).
37. Scheidt, R. A., Reinkensmeyer, D. J., Conditt, M. A., Rymer, W. Z. & Mussa-Ivaldi, F. A. Persistence of motor adaptation during constrained, multi-joint, arm movements. *J Neurophysiol* **84**, 853–862 (2000).
38. Smith, M. A., Ghazizadeh, A. & Shadmehr, R. Interacting adaptive processes with different timescales underlie short-term motor learning. *PLoS Biology* **4**, e179 (2006).
39. JASP Team, Version 0.19.1. JASP. (2024).
40. Wong, J. D., Kistemaker, D. A., Chin, A. & Gribble, P. L. Can proprioceptive training improve motor learning? *J Neurophysiol* **108**, 3313–3321 (2012).
41. von Hofsten, C. Developmental changes in the organization of prereaching movements. *Developmental Psychology* **20**, 378–388 (1984).
42. Konczak, J., Borutta, M., Topka, H. & Dichgans, J. The development of goal-directed reaching in infants: hand trajectory formation and joint torque control. *Exp Brain Res* **106**, (1995).
43. Konczak, J. & Dichgans, J. The Development of Hand Trajectory Formation and Joint Kinematics During Reaching in Infancy. in *Three-dimensional Kinematics of the Eye, Head and Limb Movements* (Routledge, 1997).
44. Schmidt, R. A. A schema theory of discrete motor skill learning. *Psychological Review* **82**, 225–260 (1975).
45. Newell, K. M. Motor Skill Acquisition. *Annual Review of Psychology* **42**, 213–237 (1991).

46. Willingham, D. B. A neuropsychological theory of motor skill learning. *Psychological Review* **105**, 558–584 (1998).

47. Atkeson, C. G. LEARNING ARM KINEMATICS AND DYNAMICS. *Annual Review of Neuroscience* **12**, 157–183 (1989).

48. Mosier, K. M., Scheidt, R. A., Acosta, S. & Mussa-Ivaldi, F. A. Remapping hand movements in a novel geometrical environment. *Journal of neurophysiology* **94**, 4362–4372 (2005).